ARTICLE

doi:10.1038/nature15247

Architecture of the mammalian mechanosensitive Piezo1 channel

Jingpeng Ge[1,2]*, Wanqiu Li[2]*, Qiancheng Zhao[1,3]*, Ningning Li[2]*, Maofei Chen[1,2], Peng Zhi[3], Ruochong Li[1,2], Ning Gao[2], Bailong Xiao[1,3,4] & Maojun Yang[1,2]

Piezo proteins are evolutionarily conserved and functionally diverse mechanosensitive cation channels. However, the overall structural architecture and gating mechanisms of Piezo channels have remained unknown. Here we determine the cryo-electron microscopy structure of the full-length (2,547 amino acids) mouse Piezo1 (Piezo1) at a resolution of 4.8 Å. Piezo1 forms a trimeric propeller-like structure (about 900 kilodalton), with the extracellular domains resembling three distal blades and a central cap. The transmembrane region has 14 apparently resolved segments per subunit. These segments form three peripheral wings and a central pore module that encloses a potential ion-conducting pore. The rather flexible extracellular blade domains are connected to the central intracellular domain by three long beam-like structures. This trimeric architecture suggests that Piezo1 may use its peripheral regions as force sensors to gate the central ion-conducting pore.

Mechanosensitive cation channels have key roles in converting mechanical stimuli into various biological activities, such as touch, hearing and blood pressure regulation, through a process termed mechanotransduction[1]. Piezo proteins have recently been identified as pore-forming subunits of the long-sought-after mechanosensitive cation channels in metazoans[2–8]. A single fly *Piezo* gene has been shown to be involved in mechanical nociception[8]. There are two Piezo proteins in vertebrates: Piezo1 and Piezo2. In vertebrates, including fish[9], birds[10], rodents[11–14] and humans[15], Piezo2 mediates gentle touch sensation. By contrast, Piezo1 has broad roles in multiple physiological processes, including sensing shear stress of blood flow for proper blood vessel development[16,17], regulating red blood cell function[18,19] and controlling cell migration and differentiation[20,21]. In humans, mutations of *PIEZO1* or *PIEZO2* have been linked to several genetic diseases, including dehydrated hereditary stomatocytosis[22–27], distal arthrogryposis type 5 (ref. 28), Gordon syndrome and Marden–Walker syndrome[29]. These findings demonstrate the functional importance of Piezo channels, as well as their pathological relevance and potential as therapeutic targets.

Despite the functional importance of Piezo proteins, their gating mechanisms and three-dimensional (3D) structures are yet to be defined. They do not bear notable sequence and structural homology to any known classes of ion channel, such as voltage- or ligand-gated channels[30–32], transient receptor potential (TRP) channels[33,34], prokaryotic mechanosensitive channels[35–38] or eukaryotic mechanosensitive two-pore-domain potassium channels[39]. Mammalian Piezo proteins contain more than 2,500 residues with numerous predicted transmembrane segments[2,3,7,40] and form homo-oligomerized channel complexes[3]. However, the exact stoichiometry, topology, architecture and functional domains involved in pore formation, force sensing and regulation remain to be solved.

Combining protein engineering, X-ray crystallography, single-particle cryo-electron microscopy and live-cell immunostaining, we have obtained the medium-resolution structure of the full-length Piezo1 channel. Our results provide key insights into the ion-conducting and gating mechanisms of this novel class of mechanosensitive ion channels.

Piezo1 forms a homotrimer

Our initial effort was focused on obtaining a sufficient amount of acceptably homogenous Piezo proteins. Human, mouse and *Drosophila* Piezo complementary DNAs, in full-length or truncated forms, were cloned into a vector encoding a carboxy-terminal (C-terminal) glutathione *S*-transferase (GST) tag with a precision protease cleavage site in between (Piezo1–pp–GST). Constructs were tested for their expression using transient transfection in HEK293T cells. A large number of detergents in various classes were screened for their compatibility with the extraction and purification of Piezo proteins. Finally, a combination of mouse Piezo1 with the detergent C12E10 was used for purification and structural determination.

Gel filtration chromatography showed that Piezo1–pp–GST and Piezo1 without the GST tag both contained two forms of oligomer, but at different ratios (Fig. 1a–c and Extended Data Fig. 1). On native gels, Piezo1–pp–GST migrated as a major band at a molecular weight of about 1,200 kDa and a minor one at about 900 kDa (Fig. 1c). This result seemed consistent with a previous study, which suggested that Piezo1 fused to GST formed a homotetramer[3]. However, examination of Piezo1–pp–GST proteins by negative-staining electron microscopy showed an ostensibly dimeric arrangement of particles (Fig. 1d, e). Two-dimensional (2D) classification of these particles indicated that the two halves were highly similar (Fig. 1f), suggesting that the dimerized GST tag may mediate further dimerization of Piezo1 complexes. Consistent with this possibility, Piezo1 with the GST tag cleaved displayed mainly a molecular weight of 900 kDa on native gels (Fig. 1c). Moreover, almost no particles with the dimeric arrangement could be observed in the tag-free Piezo1 sample. Rather, particles with a three-fold symmetry were clearly detected (Fig. 1g–i). As a further confirmation, Flag-tagged Piezo1 displayed a major band at about 900 kDa on native gels (Fig. 1c). Thus, our data suggest that the major oligomeric state of the purified Piezo1 is trimeric. The majority of

[1]Tsinghua-Peking Joint Center for Life Sciences, School of Life Sciences or Medicine, Tsinghua University, Beijing 100084, China. [2]Ministry of Education, Key Laboratory of Protein Sciences, School of Life Sciences, Tsinghua University, Beijing 100084, China. [3]Department of Pharmacology and Pharmaceutical Sciences, School of Medicine, Tsinghua University, Beijing 100084, China. [4]IDG/McGovern Institute for Brain Research, Tsinghua University, Beijing 100084, China.
*These authors contributed equally to this work.

©2015 Macmillan Publishers Limited. All rights reserved

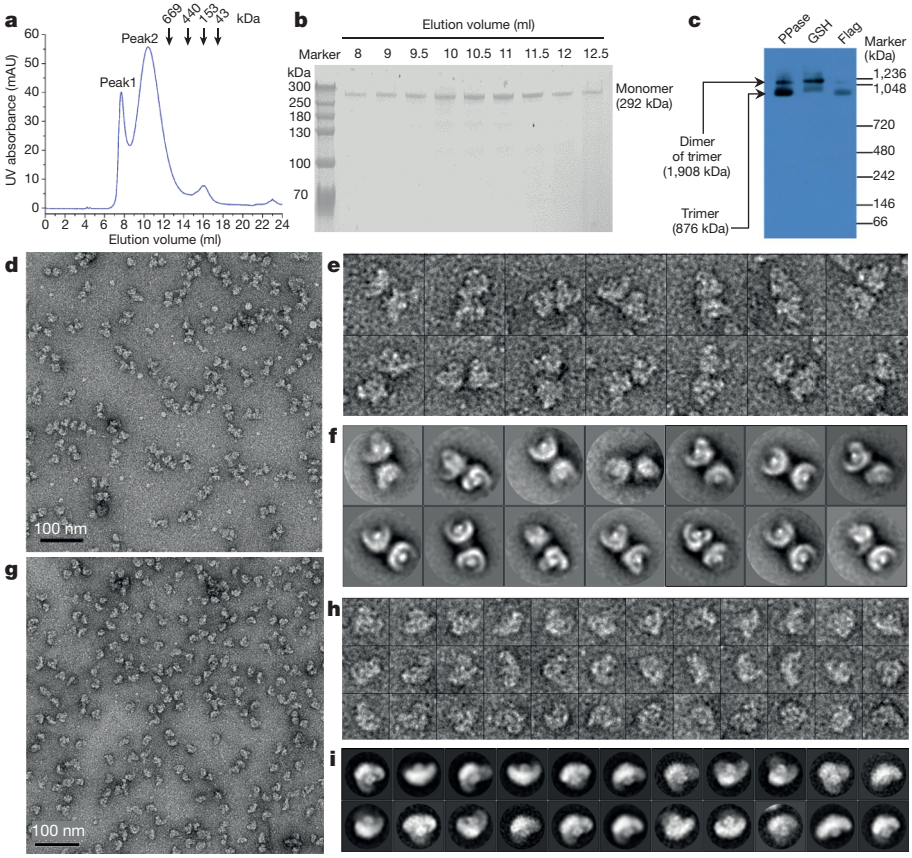

Figure 1 | Piezo1 forms a homotrimer. **a**, A representative trace of gel filtration of the full-length Piezo1, with molecular weight markers indicated. UV, ultraviolet. **b**, Protein samples of the indicated fractions were subjected to SDS–PAGE and Coomassie blue staining. **c**, Native gel and western blotting analysis of GST-cleaved Piezo1 (PPase), Piezo1–pp–GST (GSH) and Piezo1–Flag (Flag) samples with an anti-Piezo1 antibody. **d**, A representative micrograph of the negatively stained Piezo1–pp–GST. **e**, Raw particles of Piezo1–pp–GST. **f**, 2D class averages of Piezo1–pp–GST particles. **g**, A representative micrograph of the negatively stained Piezo1. **h**, Raw particles of Piezo1. **i**, 2D class averages of Piezo1 particles.

Piezo1–pp–GST fusion proteins form a dimer of trimers, as a result of the dimerized GST tags.

The unusual migration of the 1,900-kDa Piezo1–pp–GST dimer of trimers near the 1,200-kDa marker might have led to the incorrect characterization of Piezo1–pp–GST as a tetramer in the previous report[3]. The large native size of the protein, together with its numerous transmembrane segments, might have resulted in its unusual mobility on native gels owing to the influence of the detergents. Nevertheless, we could not completely exclude the possibility that Piezo1 exists in other oligomeric states on the membrane or under different conditions *in vitro*, a scenario observed in previous studies of other ion channels (for example, Orai channels)[41,42].

Three-blade, propeller-shaped Piezo1 homotrimer

Using a single-particle approach during cryo-electron microscopy, we determined the trimeric structure of Piezo1 (Fig. 2a–d and Extended Data Figs 2–5). Notably, the density map revealed that Piezo1 formed a three-blade, propeller-shaped architecture, with distinct regions resembling the typical structural components of a propeller, including three blades and a central cap. Viewed from the top, the diameter and the axial height of the structure are 200 Å and 155 Å, respectively (Fig. 2d). The transmembrane region could be readily located and contains many paired density rods, in good agreement with the 2D analyses (Fig. 2c–f). The transmembrane region contains three extended and twisted arrays of transmembrane helices (Fig. 2f, second from left). Beyond the transmembrane helical array, three thick distal blades are arranged in a superhelical fashion and each blade also has a helicoidal surface (Fig. 2d, e and f, second from right). A single central cap sits above the surface of the transmembrane core with a gap (~8 Å) in between (Fig. 2e). Furthermore, a tightly packed region, likely to be a compact soluble domain, is located on the opposite side of the cap, right below the transmembrane region (Fig. 2e). Three long, distinct density rods exposed on the outer surface of the transmembrane region, hereafter termed beam, seem to connect the distal end of the transmembrane region and the blades mechanically to the centre of the trimeric complex at the bottom face. The diameter of the density rod suggests that the beam is composed of a two-stranded coiled coil (Fig. 2d, e).

Topology determination

The proposed detachment of the cap from the transmembrane core indicates that it is likely to be a soluble region. A topological prediction model suggests that residues from 2210 to 2457 (termed the C-terminal extracellular domain, CED) constitute a large extracellular loop followed by the last transmembrane segment at the C terminus[43]. To test whether this region constitutes the cap, we constructed and purified the deletion-mutant Piezo1(Δ2219–2453) and examined it by negative-staining electron microscopy. 2D classification of Piezo1(Δ2219–2453) particles revealed the central cap was absent in 2D class averages (Extended Data Fig. 6a, b), confirming that this region indeed forms the cap.

Next, we solved the crystal structure of the CED (Piezo1(2214–2457)) (Fig. 2g and Extended Data Table 1), which was similar to that of the same region of *Caenorhabditis elegans* Piezo reported recently[43]. The root-mean-square deviation of 181 aligned α-carbon atoms between these two structures is 1.7 Å (Extended Data Fig. 6c, d). The amino (N) and C termini of the CED are on the same side and close to each other (Fig. 2g), consistent with the topological prediction[40,43] that the CED is located between the last two transmembrane segments in the C-terminal region of Piezo1.

The CED formed a trimer in both gel filtration and crystal lattice (Extended Data Fig. 6d, e). A direct and rigid fitting of the crystallographic trimer of the CED into the cryo-electron microscopy density map resulted in a match, with a correlation coefficient of 0.89 (Extended Data Fig. 6f). These results demonstrate that the cap is formed by a CED trimer, further supporting the conclusion that the full-length Piezo1 forms a homotrimer. Furthermore, the high consistency between the crystal structure and the cryo-electron

©2015 Macmillan Publishers Limited. All rights reserved

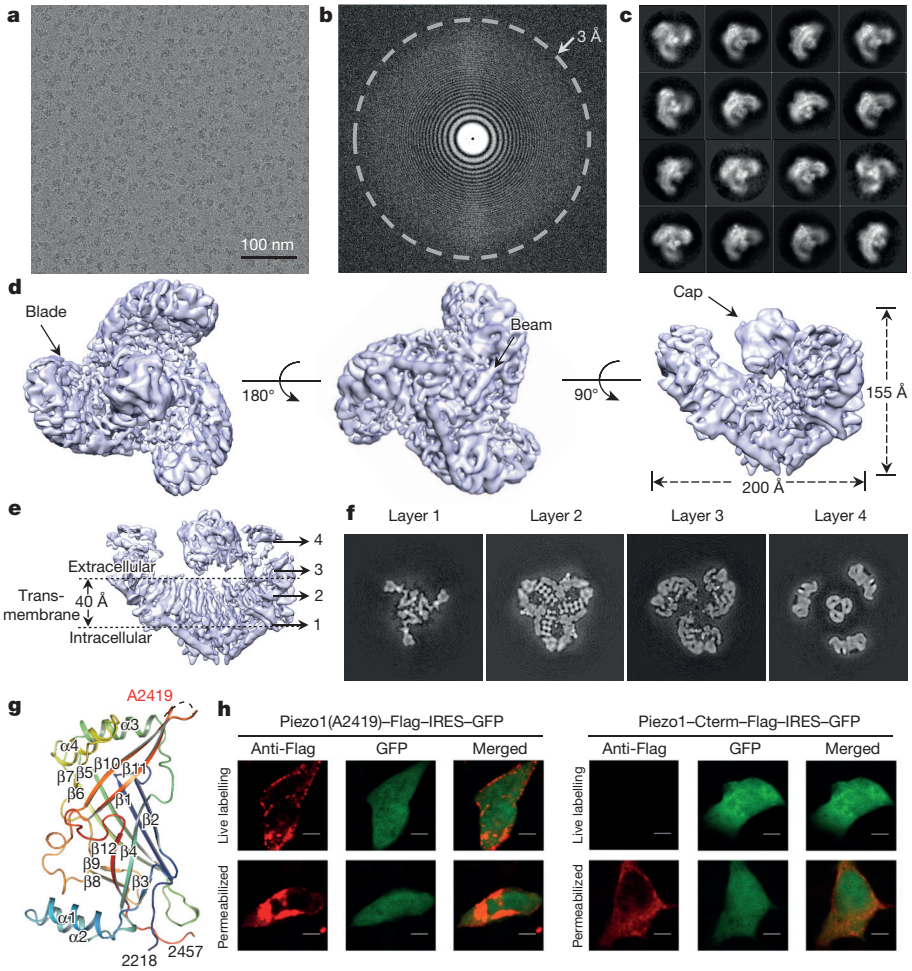

Figure 2 | Overall structure of Piezo1. **a**, A representative cryo-electron micrograph of Piezo1. **b**, Power spectrum of the micrograph in **a**, with the 3-Å frequency indicated. **c**, Representative 2D class averages of Piezo1 particles, showing fine features of the trimeric complex. **d**, Top, bottom and side views of an unsharpened map (5σ contour level) of Piezo1, with distinct regions labelled. The dimensions of the trimeric structure is shown in the rightmost panel. **e**, Side view of the sharpened map (6σ contour level) of Piezo1 filtered to a resolution of 4.8 Å, with the transmembrane region indicated. **f**, Selected *z*-slices of the final sharpened map corresponding to the layers indicated by the numbered arrows in **e**. **g**, The cartoon model of the crystal structure of a single C-terminal extracellular domain. The dashed line indicates the missing residues. The Flag tag was inserted after residue A2419. **h**, Immunostaining of cells transfected with the indicated constructs with an anti-Flag antibody either in live labelling (top row) or after fixation and permeabilization (bottom row). Scale bars, 10 μm. GFP, green fluorescent protein; IRES, internal ribozyme entry site.

microscopy map of the cap domain confirmed the correctness of the density map and determined the handedness of the map.

To further confirm the topological location of the CED and the C terminus of Piezo1, we performed immunolabelling of live HEK293T cells expressing Piezo1 with a Flag tag fused either in a flexible loop of the CED (after A2419) or at the C terminus of Piezo1. Using confocal microscopy, we found that the Flag tag could be labelled on the plasma membrane of live cells only when inserted in the CED and not at the C terminus (Fig. 2h). These data demonstrate that the CED is an extracellular domain, whereas the C terminus is intracellular, consistent with a recent report[40]. Consequently, this suggests that both the central cap and the three blades locate at the extracellular side, whereas the beams locate at the intracellular side.

The transmembrane skeleton

Piezo proteins have been predicted to contain an unusually large number of transmembrane segments (about 30–40) in one molecule[2,3,7,40]. Several potential topology models of Piezo have recently been proposed, with the number of transmembrane segments ranging from 10 to 38 (ref. 40). The local resolution of the cryo-electron microscopy density map shows that the transmembrane region is associated with a higher resolution, which allowed us to build a *de novo* alanine model with 492 amino acids for the more readily identified transmembrane segments, beam and the intracellular C-terminal domain (CTD). Together with the 227 amino acids of the CED, we built a total of 719 residues (out of 2,547 amino acids) for each monomer (Fig. 3a and Extended Data Figs 7, 8). The whole transmembrane skeleton displays a three-winged arrangement, with each extended wing being slightly twisted (Fig. 3b). From the map, 14 transmembrane segments could be readily recognized on each wing. A potential topology of at least 14 transmembrane segments for each protomer is consistent with a recent topology model of 18 transmembrane segments, instead of 38 transmembrane segments[40]. In line with this observation, a single blade has a volume comparable to the cap region, which is made up of about 700 residues. Thus, some of the predicted N-terminal helices should reside in the distal extracellular regions.

To facilitate the description of our structure and based on known features of ion channels, we refer to the core transmembrane segments as inner helix (IH) and outer helix (OH) and to the peripheral transmembrane arrays as peripheral helix (PH) (Fig. 3). The 12 PHs from the same monomer are organized as six helical pairs, extending from the central axis to the periphery of the complex (Fig. 3b). They are connected to the extracellular blade. The density for the connecting sequences from PH1 to PH7 allowed us to make tentative connections between them, except for the connection between PH4 and PH5 (Extended Data Fig. 8a).

Main-chain tracing of the PH1, IH and OH towards the transmembrane core in the density map, together with the information from topology (Fig. 3c) and secondary structure prediction (Extended Data Fig. 9), allowed us to map these three transmembrane segments on the primary sequence and assign some of the linker sequences between them into the corresponding density features. These analyses suggest that the OH connects to PH1 through four continuous α-helices, which form a unique hairpin structure at the interface of two adjacent subunits. This hairpin structure, termed the anchor, penetrates into the inner leaflet of the membrane, with a long helix ($\alpha4^{anchor}$) roughly parallel to the membrane (Fig. 3a, right and Extended Data Fig. 8b). The remaining density features in the map include the IH and its connecting density (also four α-helices) all the way to the intracellular surface of the channel, suggesting that the IH is the last

©2015 Macmillan Publishers Limited. All rights reserved

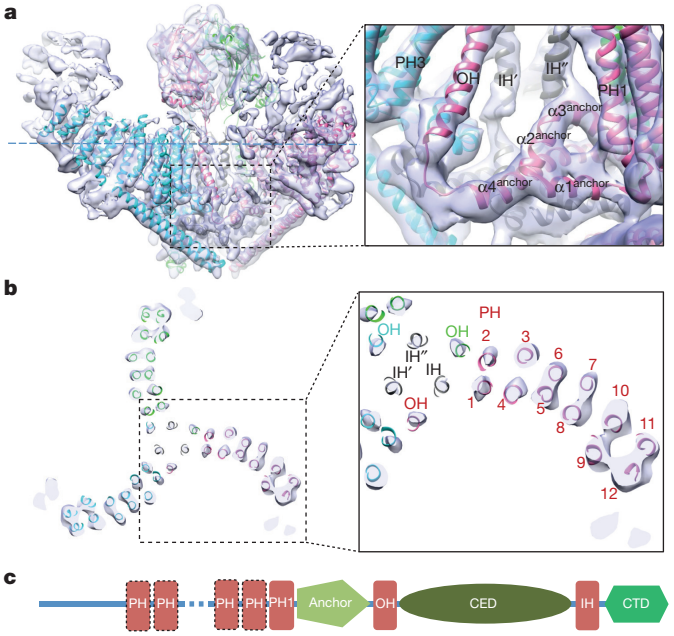

Figure 3 | Organization of the transmembrane skeleton. **a**, A side view of the cryo-electron microscopy density map superimposed with separately coloured poly-alanine models of each subunit. The boxed region is enlarged to illustrate the anchor domain. **b**, A *z*-slice representation of the overall organization of the transmembrane skeleton of the layer indicated by the blue dashed line in **a**. The boxed region is amplified to illustrate the central transmembrane core that consists of three IHs and three OHs and wings of the peripheral helices (PH1–PH12). Owing to the ambiguity in the connection, the three IHs are not assigned to each subunit and thus labelled as IH, IH′ and IH″. **c**, The model represents the topology of the C-terminal part of Piezo1. Different structural units are indicated.

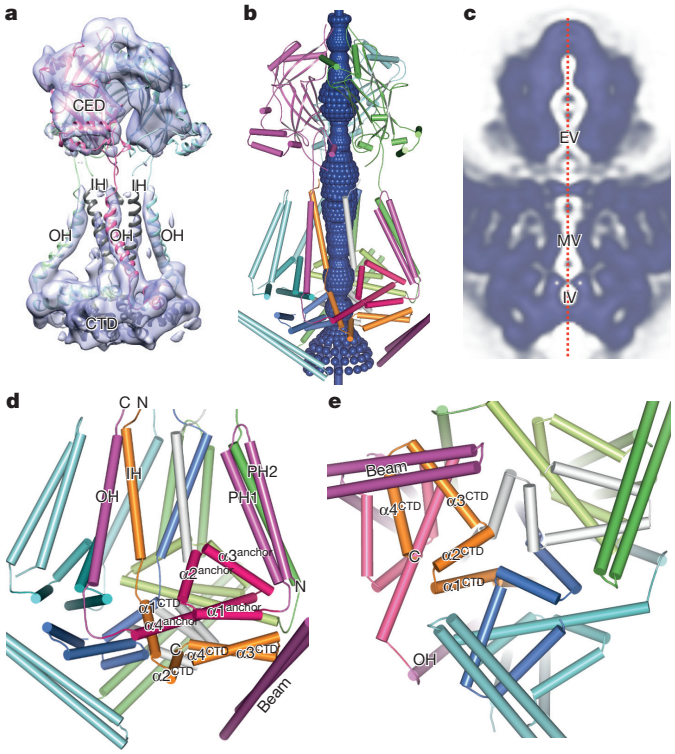

Figure 4 | Putative ion-conducting pore. **a**, Surface representation (transparent) of the segmented map of the putative pore module, including the OH, CED, IH and CTD. **b**, Same as a, but the model is superimposed with the putative ion-conducting pore (deep blue), produced by HOLE[48] with the poly-alanine model and the CED crystal structure. **c**, Central slice of the rotationally averaged density map, highlighting a continuous central pore along the *z*-axis (red dotted line). The extracellular vestibule (EV), transmembrane vestibule (MV) and intracellular vestibule (IV) regions are labelled. **d**, A side view of the CTD and the pore module consisting of the OH, IH and the CTD helices. **e**, Same as d, but viewed from the intracellular side.

transmembrane segment from the C terminus. In line with this assignment, the intracellular C terminus is located at the centre of the intracellular side, as indicated by the location of the C-terminal GST tag in Piezo1–pp–GST.

Together with the finding that the CED is inserted between the last two transmembrane segments from the C terminus, the OH is likely to be the second-to-last transmembrane segment from the C terminus, because of the close distance (matching the length of the linker sequences) between the N terminus of the CED and the extracellular end of the OH (Fig. 3a and Extended Data Fig. 9). In addition, the distance constraint enabled us to put a connection between a specific OH and one of the three N termini of the CED domain. However, we cannot unambiguously connect a specific IH to the three possible C termini of the CED.

Nevertheless, with the primary sequence of the PH1–anchor–OH–CED from one monomer fixed in the density map, a clear separation of the three subunits on the 3D structure could be achieved (Fig. 3a). The presence of the anchor domain also seems to result in a clockwise swapping of the OH–CED of one monomer (viewed from the cap) into a region of the neighbouring monomer. This helix-swapping arrangement might be critical for the stabilization of the Piezo1 trimer. Although unambiguous sequence assignment at the residue level was not feasible, this anchor domain of Piezo1 could be mapped to residues around 2100 to 2190, a region containing the most evolutionarily conserved sequence motif, PF(X2)E(X6)W (2129–2140), among Piezo homologues (Extended Data Fig. 9)[44]. The disease-causing mutation Piezo1(T2142) (T2127 of PIEZO1 in humans)[23] is located in this region, supporting the functional relevance of the anchor. Another mutation targeting this motif, Piezo1(E2133), was found to affect the Piezo1 channel pore properties[40].

Each wing of the transmembrane region sits on a coiled-coil beam exposed at the intracellular surface. The beam is about 80 Å in length and positioned at about 30° relative to the membrane (Fig. 3a). It originates peripherally at the intracellular side of the PH7–PH8 pair and ends near the central axis of the trimer, where it seems to interact with the anchor and the CTD (Fig. 3a). This organization suggests that the three beams might be responsible for transmitting conformational changes from peripheral transmembrane segments and the extracellular blades to the central region, where the ion-conducting pore is most likely to reside.

The ion-conducting pore

The centre of the Piezo1 channel within the membrane consists of six transmembrane helices in a triangular arrangement (Fig. 3b, right and Fig. 4). Three IHs, presumably extended from the C termini of the CEDs, are located at the innermost position and seem to line a central pore. Three OHs, extended from the N termini of the CEDs, further enclose the three IHs (Fig. 4a). This central region, including the IH–OH pairs, the CEDs and the CTDs, probably comprises the pore module of Piezo1. The lack of side-chain information in the three IHs prevented us from accurately determining the radius of the pore. Nonetheless, apparent restriction sites could be readily detected, suggesting that they are potential gating positions. The central slice of the rotationally averaged density map revealed a continuous central channel along the *z*-axis, including an extracellular vestibule within the cap, a transmembrane vestibule enclosed by the three IHs and an intracellular vestibule formed by the trimeric CTD (Fig. 4b–e). The organization of the central transmembrane core and the pore is reminiscent of the trimeric $P2X_4$ channels[32] and acid-sensing ion channels[45], although they possess only two transmembrane helices

©2015 Macmillan Publishers Limited. All rights reserved

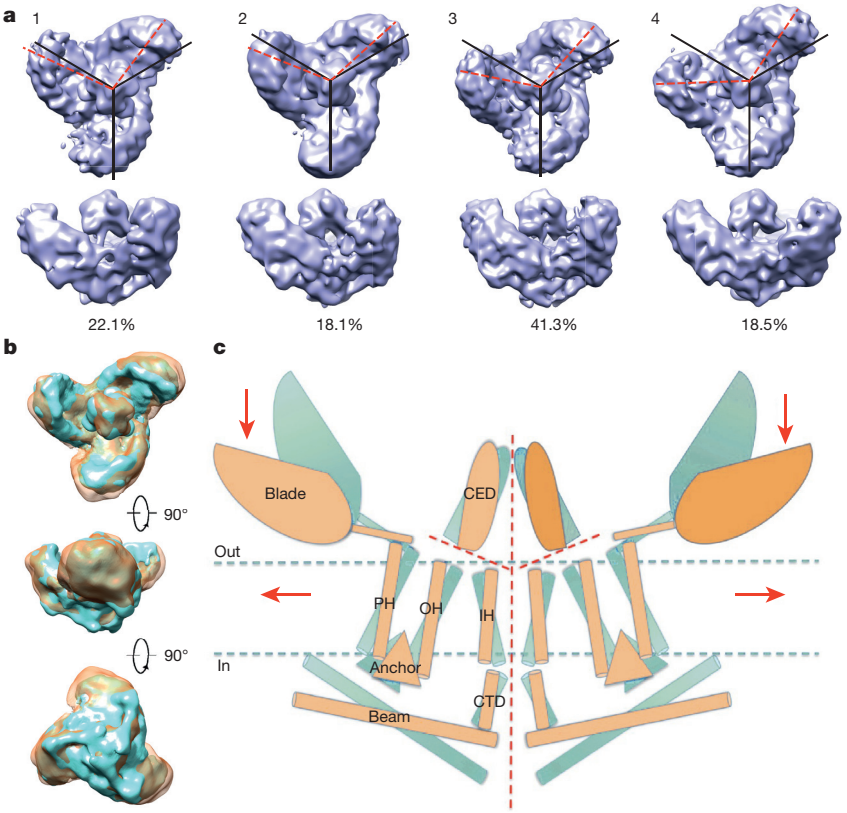

Figure 5 | Conformational heterogeneity of the 'blade' and a proposed model of force-induced gating of Piezo channels. **a**, Representative classes of Piezo1 structures from symmetry-free 3D classification. For each top-viewed structure, three black lines (120° interval) are drawn to illustrate the expected position of blades on the basis of perfect C3 symmetry. Red dashed lines represent observed positions of the blades. **b**, Structural comparison between further-refined maps of structures 4 (orange) and 3 (cyan) in **a**, showing the centripetal movement of the blades (top) and the tilted movement of the beams relative to the plasma membrane plane (bottom). **c**, Proposed model of the force-induced gating of Piezo channels. The blue and orange models represent the closed and open state channels, respectively. Red dashed lines indicate the possible ion-conduction pathways. Presumably, force-induced motion (red arrows) of the peripheral blade or PHs leads to conformational arrangement and gating of the channel.

and a large extracellular domain in each monomer. Based on this structural information, we propose that the OH–CED–IH–CTD-containing region functions as the pore module of Piezo channels (Fig. 4). According to our assignment, this pore module comprises the C-terminal region from residues 2172 to 2547. This is consistent with a recent study showing that the portion from 1974 to the C terminus of Piezo1 is essential for ion permeation properties[40].

The flexible blades as potential force sensors

The local resolution map shows that the three blades of Piezo1 have smeared densities at their distal ends and fragmented density in the sharpened map (Fig. 2d, e). In contrast, the cap, transmembrane skeleton, beam and CTD are better defined and display apparent secondary structural features. The blades of Piezo1 are highly flexible (Figs 2c, 3a and Extended Data Fig. 8). Indeed, comparison of different classes of the structures from symmetry-free 3D classification reveals several motion modes for the blade (Fig. 5a, b and Extended Data Fig. 5a). The most notable one is that the rotational spacing between two adjacent blades varies from 100° to 140° (Fig. 5a). Other less pronounced but identifiable conformational variations include the tilting of the blade relative to the plasma membrane and curvature changes on the helicoidal surface (Fig. 5b). Further supporting the structural flexibility of the blade regions, subregion refinement (see Methods) considerably improved the densities of the cap, but not that of the blade. The large conformational heterogeneity in the blades could be the main factor hampering high-resolution structural refinement of the entire structure. However, the structural flexibility of the propeller-like blades could be functionally meaningful. For example, they might serve as sensors of mechanical force exerted on the channel, thus contributing to mechanical gating of Piezo1 (Fig. 5c).

The recently resolved cryo-electron microscopy structure of human TRPA1 reveals a fourfold propeller-like structure composed of numerous ankyrin repeats[33]. Although TRPA1 alone is not sufficient to mediate mechanosensitive currents, it has been proposed to mediate slowly adapting mechanically activated currents in somatosensory neurons[46,47], raising an intriguing possibility that TRPA1 may employ the propeller-like structure to confer mechanosensitivity under certain circumstances. It remains possible that other extracellular or intracellular proteins may interact with and regulate Piezo channels. These hypotheses merit further investigation.

Conclusions

The medium-resolution cryo-electron microscopy structure of Piezo1 provides critical insights into the general architecture, oligomerization state and topological organization of Piezo channels. Our putative assignment of the central ion-conducting pore, mechanosensing and transduction components serves as a testable framework for dissection of the structure and mechanism of this class of channels.

Online Content Methods, along with any additional Extended Data display items and Source Data, are available in the online version of the paper; references unique to these sections appear only in the online paper.

Received 26 March; accepted 24 July 2015.
Published online 21 September, corrected online 4 November 2015 (see full-text HTML version for details).

1. Chalfie, M. Neurosensory mechanotransduction. *Nature Rev. Mol. Cell Biol.* **10,** 44–52 (2009).
2. Coste, B. *et al.* Piezo1 and Piezo2 are essential components of distinct mechanically activated cation channels. *Science* **330,** 55–60 (2010).
3. Coste, B. *et al.* Piezo proteins are pore-forming subunits of mechanically activated channels. *Nature* **483,** 176–181 (2012).
4. Nilius, B. & Honoré, E. Sensing pressure with ion channels. *Trends Neurosci.* **35,** 477–486 (2012).
5. Volkers, L., Mechioukhi, Y. & Coste, B. Piezo channels: from structure to function. *Pflugers Arch.* **467,** 95–99 (2015).
6. Bae, C., Gottlieb, P. A. & Sachs, F. Human PIEZO1: removing inactivation. *Biophys. J.* **105,** 880–886 (2013).
7. Gottlieb, P. A. & Sachs, F. Piezo1: properties of a cation selective mechanical channel. *Channels* **6,** 214–219 (2012).
8. Kim, S. E., Coste, B., Chadha, A., Cook, B. & Patapoutian, A. The role of *Drosophila* Piezo in mechanical nociception. *Nature* **483,** 209–212 (2012).
9. Faucherre, A., Nargeot, J., Mangoni, M. E. & Jopling, C. *piezo2b* regulates vertebrate light touch response. *J. Neurosci.* **33,** 17089–17094 (2013).
10. Schneider, E. R. *et al.* Neuronal mechanism for acute mechanosensitivity in tactile-foraging waterfowl. *Proc. Natl Acad. Sci. USA* **111,** 14941–14946 (2014).

©2015 Macmillan Publishers Limited. All rights reserved

11. Maksimovic, S. *et al.* Epidermal Merkel cells are mechanosensory cells that tune mammalian touch receptors. *Nature* **509,** 617–621 (2014).
12. Woo, S. H. *et al.* Piezo2 is required for Merkel-cell mechanotransduction. *Nature* **509,** 622–626 (2014).
13. Ranade, S. S. *et al.* Piezo2 is the major transducer of mechanical forces for touch sensation in mice. *Nature* **516,** 121–125 (2014).
14. Ikeda, R. *et al.* Merkel cells transduce and encode tactile stimuli to drive Aβ-afferent impulses. *Cell* **157,** 664–675 (2014).
15. Schrenk-Siemens, K. *et al.* PIEZO2 is required for mechanotransduction in human stem cell-derived touch receptors. *Nature Neurosci.* **18,** 10–16 (2015).
16. Ranade, S. S. *et al.* Piezo1, a mechanically activated ion channel, is required for vascular development in mice. *Proc. Natl Acad. Sci. USA* **111,** 10347–10352 (2014).
17. Li, J. *et al.* Piezo1 integration of vascular architecture with physiological force. *Nature* **515,** 279–282 (2014).
18. Faucherre, A., Kissa, K., Nargeot, J., Mangoni, M. E. & Jopling, C. Piezo1 plays a role in erythrocyte volume homeostasis. *Haematologica* **99,** 70–75 (2014).
19. Cahalan, S. M. *et al.* Piezo1 links mechanical forces to red blood cell volume. *eLife* **4,** 07370 (2015).
20. McHugh, B. J. *et al.* Integrin activation by Fam38A uses a novel mechanism of R-Ras targeting to the endoplasmic reticulum. *J. Cell Sci.* **123,** 51–61 (2010).
21. Pathak, M. M. *et al.* Stretch-activated ion channel Piezo1 directs lineage choice in human neural stem cells. *Proc. Natl Acad. Sci. USA* **111,** 16148–16153 (2014).
22. Albuisson, J. *et al.* Dehydrated hereditary stomatocytosis linked to gain-of-function mutations in mechanically activated PIEZO1 ion channels. *Nature Commun.* **4,** 1884 (2013).
23. Andolfo, I. *et al.* Multiple clinical forms of dehydrated hereditary stomatocytosis arise from mutations in *PIEZO1*. *Blood* **121,** 3925–3935 (2013).
24. Bae, C., Gnanasambandam, R., Nicolai, C., Sachs, F. & Gottlieb, P. A. Xerocytosis is caused by mutations that alter the kinetics of the mechanosensitive channel PIEZO1. *Proc. Natl Acad. Sci. USA* **110,** E1162–E1168 (2013).
25. Beneteau, C. *et al.* Recurrent mutation in the PIEZO1 gene in two families of hereditary xerocytosis with fetal hydrops. *Clin. Genet.* **85,** 293–295 (2014).
26. Shmukler, B. E. *et al.* Dehydrated stomatocytic anemia due to the heterozygous mutation R2456H in the mechanosensitive cation channel PIEZO1: a case report. *Blood Cells Mol. Dis.* **52,** 53–54 (2014).
27. Zarychanski, R. *et al.* Mutations in the mechanotransduction protein PIEZO1 are associated with hereditary xerocytosis. *Blood* **120,** 1908–1915 (2012).
28. Coste, B. *et al.* Gain-of-function mutations in the mechanically activated ion channel PIEZO2 cause a subtype of distal arthrogryposis. *Proc. Natl Acad. Sci. USA* **110,** 4667–4672 (2013).
29. McMillin, M. J. *et al.* Mutations in *PIEZO2* cause Gordon syndrome, Marden–Walker syndrome, and distal arthrogryposis type 5. *Am. J. Hum. Genet.* **94,** 734–744 (2014).
30. Zhang, X. *et al.* Crystal structure of an orthologue of the NaChBac voltage-gated sodium channel. *Nature* **486,** 130–134 (2012).
31. Payandeh, J., Scheuer, T., Zheng, N. & Catterall, W. A. The crystal structure of a voltage-gated sodium channel. *Nature* **475,** 353–358 (2011).
32. Kawate, T., Michel, J. C., Birdsong, W. T. & Gouaux, E. Crystal structure of the ATP-gated P2X(4) ion channel in the closed state. *Nature* **460,** 592–598 (2009).
33. Paulsen, C. E., Armache, J. P., Gao, Y., Cheng, Y. & Julius, D. Structure of the TRPA1 ion channel suggests regulatory mechanisms. *Nature* **520,** 511–517 (2015).
34. Liao, M., Cao, E., Julius, D. & Cheng, Y. Structure of the TRPV1 ion channel determined by electron cryo-microscopy. *Nature* **504,** 107–112 (2013).
35. Liu, Z., Gandhi, C. S. & Rees, D. C. Structure of a tetrameric MscL in an expanded intermediate state. *Nature* **461,** 120–124 (2009).
36. Bass, R. B., Strop, P., Barclay, M. & Rees, D. C. Crystal structure of *Escherichia coli* MscS, a voltage-modulated and mechanosensitive channel. *Science* **298,** 1582–1587 (2002).
37. Chang, G., Spencer, R. H., Lee, A. T., Barclay, M. T. & Rees, D. C. Structure of the MscL homolog from *Mycobacterium tuberculosis*: a gated mechanosensitive ion channel. *Science* **282,** 2220–2226 (1998).
38. Kung, C., Martinac, B. & Sukharev, S. Mechanosensitive channels in microbes. *Annu. Rev. Microbiol.* **64,** 313–329 (2010).
39. Brohawn, S. G., del Mármol, J. & MacKinnon, R. Crystal structure of the human K2P TRAAK, a lipid- and mechano-sensitive K^+ ion channel. *Science* **335,** 436–441 (2012).
40. Coste, B. *et al.* Piezo1 ion channel pore properties are dictated by C-terminal region. *Nature Commun.* **6,** 7223 (2015).
41. Hou, X., Pedi, L., Diver, M. M. & Long, S. B. Crystal structure of the calcium release-activated calcium channel Orai. *Science* **338,** 1308–1313 (2012).
42. Penna, A. *et al.* The CRAC channel consists of a tetramer formed by Stim-induced dimerization of Orai dimers. *Nature* **456,** 116–120 (2008).
43. Kamajaya, A., Kaiser, J. T., Lee, J., Reid, M. & Rees, D. C. The structure of a conserved Piezo channel domain reveals a topologically distinct β sandwich fold. *Structure* **22,** 1520–1527 (2014).
44. Prole, D. L. & Taylor, C. W. Identification and analysis of putative homologues of mechanosensitive channels in pathogenic protozoa. *PLoS One* **8,** e66068 (2013).
45. Gonzales, E. B., Kawate, T. & Gouaux, E. Pore architecture and ion sites in acid-sensing ion channels and P2X receptors. *Nature* **460,** 599–604 (2009).
46. Vilceanu, D. & Stucky, C. L. TRPA1 mediates mechanical currents in the plasma membrane of mouse sensory neurons. *PLoS One* **5,** e12177 (2010).
47. Kwan, K. Y., Glazer, J. M., Corey, D. P., Rice, F. L. & Stucky, C. L. TRPA1 modulates mechanotransduction in cutaneous sensory neurons. *J. Neurosci.* **29,** 4808–4819 (2009).
48. Smart, O. S., Goodfellow, J. M. & Wallace, B. A. The pore dimensions of gramicidin A. *Biophys. J.* **65,** 2455–2460 (1993).

Acknowledgements We thank H. Yu and J. Chai for discussion and proofreading of the manuscript. We thank the staff at beamline BL17U of the Shanghai Synchrotron Radiation Facility (SSRF) and beamline 3W1A of the Beijing Synchrotron Radiation Facility (BSRF) for their assistance in data collection. K. Wu and H. Wang are acknowledged for technique help. We also thank the National Center for Protein Sciences (Beijing, China) for technical support with cryo-electron microscopy data collection and for computation resources. This work was supported by grants from the Ministry of Science and Technology (2012CB911101 and 2011CB910502 to M.Y., 2015CB910102 to B.X. and 2013CB910404 to N.G.), the National Natural Science Foundation of China (21532004, 31570733, 31030020 and 31170679 to M.Y., 31422016 to N.G. and 31422027 to B.X.) and the Ministry of Education (the Young Thousand Talent program to B.X.).

Author Contributions M.Y. directed the study. J.G., M.C. and R.L. performed protein purification, detergent screening and crystallization. W.L. performed electron microscopy sample preparation, data collection and structural determination with N.L; Q.Z. was responsible for molecular cloning (with P.Z.), protein purification, detergent screening and biochemical and confocal imaging studies. N.G. directed electron microscopy studies and wrote part of the manuscript. B.X. initiated the project and directed molecular cloning, protein expression and purification and wrote most of the manuscript. All authors contributed to discussion of the data and editing of the manuscript.

Author Information The 3D cryo-electron microscopy density map has been deposited in the Electron Microscopy Data Bank (EMDB), with accession code EMD-6343. The coordinates of atomic models have been deposited in the Protein Data Bank (PDB) under the accession codes 4RAX for the CED and 3JAC for the full length. Reprints and permissions information is available at www.nature.com/reprints. The authors declare no competing financial interests. Readers are welcome to comment on the online version of the paper. Correspondence and requests for materials should be addressed to N.G. (ninggao@tsinghua.edu.cn), B.X. (xbailong@biomed.tsinghua.edu.cn) and M.Y. (maojunyang@tsinghua.edu.cn).

©2015 Macmillan Publishers Limited. All rights reserved

METHODS

No statistical methods were used to predetermine sample size, the experiments were not randomized and the investigators were not blinded to allocation during experiments and outcome assessment.

Molecular cloning. The pcDNA3.1-Piezo1-pp (PPase, PreScission protease cleavage site) -GST-IRES-GFP construct was subcloned by inserting the coding sequence of the PreScission protease cleavage site between Piezo1 (E2JF22, UniprotKB entry) and GST coding sequences in the parental construct of pcDNA3.1-Piezo1-GST-IRES-GFP[3]. Piezo1-Cterm-Flag-IRES-GFP was subcloned by inserting the synthesized double-stranded DNA fragment encoding Flag between the Piezo1-coding sequence and IRES-GFP using the restriction enzymes AscI and SacII. Piezo1(A2419)-Flag-IRES-GFP was constructed using a one-step cloning kit (Vazyme Biotech) by introducing the Flag-tag coding sequence after the residue Piezo1(A2419) into the Piezo1-GST-IRES-GFP construct and the Piezo1(Δ2219–2453) construct was generated by deleting amino acids 2219–2453 from the Piezo1-pp-GST-IRES-GFP construct. The coding sequence of the CED of Piezo1 (residues 2214–2457) was cloned into a pET22b (Novagen) vector with a C-terminal 6×His tag using the restriction enzymes NdeI and XhoI. All the constructs were confirmed by sequencing.

Protein expression and purification of Piezo1 and Piezo1(Δ2219–2453). HEK293T cells were grown in DMEM (basic) with 10% FBS. When the density of cells cultured in 150 mm × 25 mm dishes reached 80–90%, the expression plasmids were transiently transfected with polyethylenimines (Polysciences). The protein purification procedure was slightly modified from similar previously described methods[3]. After 48 h, the transfected cells were collected, washed twice with PBS and homogenized in buffer A, containing 25 mM Na-PIPES, pH 7.2, 140 mM NaCl, 2 mM dithiothreitol (DTT), detergents CHAPS (1%) and C12E9 (0.1%), 0.5% (w/v) L-α-phosphatidylcholine (Avanti) and a cocktail of protease inhibitors (Roche) at 4 °C for 1 h. After centrifugation at 100,000*g* for 40 min, the supernatant was collected and incubated with glutathione–sepharose beads (GE Healthcare) at 4 °C for 3 h. The resin was washed extensively with buffer B, containing 25 mM Na-PIPES, pH 7.2, 140 mM NaCl, 2 mM DTT, 0.1% (w/v) C12E9 and 0.01% (w/v) L-α-phosphatidylcholine. The GST-free or GST-tagged Piezo1 was cleaved off by PreScission Protease (Amersham-GE) in buffer B at 4 °C overnight or directly eluted from the protein-loaded resin with buffer B plus 10 mM GSH, respectively, and applied to size-exclusion chromatography (Superpose-6 10/300 GL, GE Healthcare) in buffer C (25 mM Na-PIPES, pH 7.2, 140 mM NaCl, 2 mM DTT) plus 0.026% (w/v) C12E10 or other detergents in the final concentration of 2× critical micelle concentration. For amphipol-bound Piezo1, amphipols were substituted for detergents as described[34], after which the protein was loaded on a Superpose-6 column in buffer C. Proteins with different kinds of detergents or amphipols were examined by both gel filtration and negative staining. Peak fractions representing oligomeric Piezo1 were collected for electron microscopy analysis. Protein in C12E10 was used for final cryo-electron microscopy structure determination. All detergents and amphipols used in this project were purchased from Anatrace.

Expression and purification of Piezo1 CED fragment. Overexpression of Piezo1 CED was induced in *Escherichia coli* BL21 strain by 0.5 mM isopropyl-β-D-thiogalactoside when the cell density reached an optical density of ~0.8 at 600 nm. After growing at 18 °C for 12 h, the cells were collected, washed, resuspended in buffer D, containing 25 mM Tris-HCl, pH 8.0, 500 mM NaCl and 20 mM imidazole, and lysed by sonication. The lysates were clarified by centrifugation at 23,000*g* for 1 h and the supernatant was collected and loaded onto Ni^{2+}-nitrilotriacetate affinity resin (Ni-NTA, Qiagen). The resin was washed extensively with buffer D and eluted with buffer D plus 280 mM imidazole. The eluate was concentrated and subjected to gel filtration (Superdex-200, GE Healthcare) with buffer E, containing 25 mM Tris-HCl, pH 8.0, 200 mM NaCl, 2 mM DTT, or buffer F, containing 25 mM Tris-HCl, pH 8.0, 25 mM NaCl and 2 mM DTT (Extended Data Fig. 6e).

NativePAGE Novex Bis-Tris gel and western blotting. The purified Piezo1 proteins were subjected to 3–12% NativePAGE Novex Bis-Tris gel for native electrophoresis according to the manufacturer's protocol at 150 V for 2 h. The native gel was transferred to a positively charged nylon/nitrocellulose membrane at 100 V for 1.5 h. After incubating in 8% (v/v) acetic acid to fix the proteins, air drying and rewetting with methanol, the membrane was blocked with 5% (w/v) milk in TBS buffer with 0.1% (w/v) Tween-20 (TBST buffer) at room temperature (~26 °C) for 1 h. The membrane was then incubated with the anti-Piezo1 antibody (1:1,000) (custom generated using the peptide YIRAPNGPEANPVK) at room temperature for 1 h, followed by washing with TBST buffer and further incubated with anti-rabbit IgG antibody (1:10,000) at room temperature for 1 h. Proteins were detected with the SuperSignal West Pico Chemiluminescent Substrate (Thermo).

Immunostaining. For live-cell labelling, cells grown on coverslips were incubated with the anti-Flag antibody (1:100, Sigma) diluted in prewarmed culture medium at room temperature for 1 h. After three washes, cells were incubated with the Alexa Fluor 594 donkey-anti-mouse IgG secondary antibody (1:200, Life Technologies) at room temperature for 1 h and then washed and fixed with 4% (w/v) paraformaldehyde. For permeabilized staining, cells were first fixed with 4% (w/v) paraformaldehyde and permeabilized with 0.2% (w/v) Triton X-100, then incubated with the anti-Flag antibody (1:200, Sigma) or the anti-GST antibody (1:200, Millipore) at room temperature for 1 h. Cells were washed and then incubated with the Alexa Fluor 594 donkey-anti-mouse IgG (1:200, Life Technologies) or Alexa Fluor 594 donkey-anti-rabbit IgG (1:200, Life Technologies) secondary antibody at room temperature for 1 h. After washing, coverslips were mounted and imaged using a Nikon A1 confocal microscope with a 60× oil objective (N.A. = 1.49) at either the GFP (488-nm exciting wavelength) or the TRITC channel (561-nm exciting wavelength).

Crystallization, data collection and structure determination of the CED. Crystals of CED proteins were obtained at 18 °C using the sitting-drop method by mixing 1 μl protein (15 mg ml^{-1}) with 1 μl reservoir solution (0.1 M HEPES, pH 7.5, 0.2 M $MgCl_2$ and 25% w/v PEG3350). Crystals appeared after 2–3 weeks and reached full size in about a month. The crystals were cryo-protected in reservoir solution containing 15–20% glycerol and flash frozen in liquid nitrogen before data collection. Native data of CED crystals were collected at beamline BL17U of the Shanghai Synchrotron Radiation Facility (SSRF). Single-wavelength anomalous dispersion data were collected at 100 K using a MAResearch M165 charge-coupled device (CCD) detector at the Beijing Synchrotron Radiation Facility (BSRF), with the crystals soaked in 2 M NaI for 1 min. All diffraction data were processed with HKL2000 (ref. 49). Further processing was carried out using programs from the CCP4 suite (Collaborative Computational Project)[50]. The heavy-atom positions in the iodine-soaked crystal were determined using SHELXD[51]. Heavy-atom parameters were then refined and initial phases were generated in the program PHASER[52] using the single-wavelength anomalous dispersion experimental phasing module. The real-space constraints were applied to the electron density map in DM[53]. The resulting map was of sufficient quality for building the model of the CED in Coot[54]. The structures were refined with the PHENIX packages[55]. Full data collection and structure statistics are summarized in Extended Data Table 1.

Negative-staining electron microscopy. An aliquot of 4 μl Piezo1 (0.05 mg ml^{-1}) was applied to glow-discharged carbon-coated copper grids (200 mesh, Zhongjingkeyi, Beijing). After the grids were incubated at room temperature for 1 min, excessive liquid was absorbed by filter paper. Grids containing the specimen were stained by applying droplets of 2% uranyl acetate for 30 s and air dried. Micrographs were generated on a T12 microscope (FEI) operated at 120 kV, using a 4k × 4k CCD camera (UltraScan 4000, Gatan). Images of Piezo1 purified with C12E10, C12E8 and amphipol A8-35 were recorded at a nominal magnification of 68,000× and with a pixel size of 1.59 Å (Extended Data Fig. 2). Images of Piezo1(ΔCED) in C12E10 were recorded at a nominal magnification of 49,000× and with a pixel size of 2.21 Å. Micrographs of random conical tilt (RCT) pairs were taken at 50° and 0° tilt angles at a nominal magnification of 49,000×.

Cryo-electron microscopy. The detergent C12E10 was chosen for cryo-electron microscopy analysis because it produced slightly better micrographs (Extended Data Fig. 2). Aliquots of 4 μl detergent-solubilized (C12E10) Piezo1 at a concentration of 0.2 mg ml^{-1} were applied to glow-discharged 300-mesh Quantifoil R2/2 grids (Quantifoil, Micro Tools GmbH, Germany) coated with a self-made continuous thin carbon. After 15 s of waiting time, grids were blotted for 1.5 s and plunged into liquid ethane using an FEI Mark IV Vitrobot operated at 4 °C and 100% humidity. Grids were examined using a TF20 microscope (FEI) operated at 200 kV with a nominal magnification of 62,000× and images were captured on a CCD camera (Gatan) under low-dose conditions. High-resolution images were captured on a Titan Krios microscope, operated at 300 kV, with a K2 Summit direct electron detector (Gatan) in counting mode. Data acquisition was performed using UCSF-Image4 (X. Li and Y. Cheng), with a nominal magnification of 22,500×, which yields a final pixel size of 1.32 Å at object scale and with defocus ranging from −1.7 μm to −2.9 μm. The dose rate on the detector was about 8.2 counts per pixel per second, with a total exposure time of 8 s. Each micrograph stack consists of 32 frames.

Image processing. The data sets of negative-staining electron microscopy were processed with EMAN2.1 (ref. 56) and RELION[57]. Reference-free 2D classification was performed with RELION. The numbers of Piezo1 particles in the presence of C12E10, C12E8 and amphipol A8-35 are 7,279, 14,045 and 7,565, respectively. For RCT[58] data processing, particle picking and classification were performed with EMAN2.1 (ref. 56) and reconstruction of RCT classes and structural refinement from all untilted particles were performed with SPIDER[59]. The

©2015 Macmillan Publishers Limited. All rights reserved

final number of particles used in generating the initial model is 5,670. The initial 3D reference created using the RCT method is shown in Extended Data Fig. 3.

For cryo-electron microscopy (TF20) data processing, 505 micrographs were processed with SPIDER[59] and RELION[57]. Particles were picked using SPIDER, manually screened (39,555 in total) and subjected to reference-free 2D classification using RELION. A final number of 16,729 particles were used for 3D refinement using the RCT model as initial reference. To validate the 3D model, 3D refinement was also performed with a Gaussian density ball as initial reference. During refinement, both the symmetry-free (C1) and symmetry-imposed (C3) reconstructions were tested (Extended Data Fig. 3d).

For processing K2 micrographs, motion correction was applied at the micrograph level using the dosefgpu_driftcorr program (developed by X. Li) to produce average micrographs across all frames[60]. Micrograph screening, particle picking and normalization were performed with SPIDER. The program CTFFIND3 (ref. 61) was used to estimate the contrast transfer function parameters. The 2D and 3D classification and refinement were performed with RELION exclusively to avoid potential structural overfitting. Classification of raw cryo-electron microscopy particles resulted in well-resolved 2D class averages, with many secondary structural features clearly discernable. In particular, on class averages of typical side views, many pieces of rod-like densities arranged in parallel fashion could be readily identified, raising the possibility that they were transmembrane helices (Fig. 2c). A total of 179,805 particles from 1,042 micrographs were subject to a cascade of 2D and 3D classification (Extended Data Fig. 5a). During 3D classification, no symmetry was imposed. Different combinations of particles from these classes were tested in refinement. After two rounds of 3D classification, a set of adequately homogeneous particles (30,021), which best matched the C3 symmetry, was subjected to a third round of 3D classification. This resulted in generally similar class structures, with no detectable improvement on particle homogeneity. Consequently, this set of particles was used for final refinement, with the RCT model low-pass filtered to 60 Å as initial reference. Applying the C3 symmetry in the refinement resulted in an overall structure at a resolution of 10.24 Å. After the first refinement, we noted that translation parameters of particles (OriginX and OriginY in RELION) were rather large, with many particles having x or y shifts of more than 15 pixels. Particles were rewindowed from original micrographs by applying their x and y shifts. Rewindowed particles were subjected to a second round of refinement using RELION, which only marginally improved the density map. A third round of refinement was performed by applying an enlarged soft mask (Extended Data Fig. 5a) of the Piezo1 channel, which improved the overall resolution to 6.03 Å. Last, particle-based beam-induced movement correction was performed by statistical movie processing in RELION, using movie frames 2–15. This yielded a final 3D density map with an overall resolution of 5.9 Å, with regions defined by the soft mask being 4.8 Å (Extended Data Fig. 5b). All reported resolutions are based on the gold-standard FSC = 0.143 (ref. 62) and the final FSC curve (4.8 Å) was corrected for the effect of a soft mask using high-resolution noise substitution[63]. In addition, subregion refinements, as previously described for ribosomal complex structural determination[64–67], were applied to improve the local densities of interest, by using a soft mask of the cap domain, the lower central pore region and a single subunit. The subsequent reported resolutions were still in the range of 4.8–5.5 Å, but with much-improved densities for these masked regions. This led to a separation of secondary structural elements in the cap and transmembrane regions. However, in all cases, the densities at the distal 'blade' domain are fragmented and limited our further quantitative analysis. Final density maps were sharpened by a B-factor of –100 Å^2 using RELION. A local resolution map was calculated using ResMap[68]. UCSF Chimera[69] was used to fit the crystal structure of the CED to the density map of the cap domain.

Poly-alanine model and structural analysis. Main-chain tracing and building a poly-alanine model were done manually using Coot[70]. Sequence alignment was performed using Clustal W2 (ref. 71). Secondary structures were predicted with PredictProtein[72] using the full-length Piezo1 sequence. Transmembrane segments were predicted using multiple prediction web servers, including Topcons[73], TMHMM2 (ref. 74), HMMTOP[75] and Phobius[76], with their results shown as green, blue, orange and pink lines, respectively, in Extended Data Fig. 9. Sequence alignment and secondary structure prediction of Piezo1 from different species were used to aid the assignment of structural elements in the density map. Multiple rounds of model rebuilding in Coot were performed for model optimization.

49. Otwinowski, Z. & Minor, W. Processing of X-ray diffraction data collected in oscillation mode. *Methods Enzymol.* **276,** 307–326 (1997).
50. Winn, M. D. *et al.* Overview of the CCP4 suite and current developments. *Acta Crystallogr. D* **67,** 235–242 (2011).
51. Schneider, T. R. & Sheldrick, G. M. Substructure solution with SHELXD. *Acta Crystallogr. D* **58,** 1772–1779 (2002).
52. McCoy, A. J. *et al.* Phaser crystallographic software. *J. Appl. Crystallogr.* **40,** 658–674 (2007).
53. Cowtan, K. D. & Main, P. Improvement of macromolecular electron-density maps by the simultaneous application of real and reciprocal space constraints. *Acta Crystallogr. D* **49,** 148–157 (1993).
54. Emsley, P. & Cowtan, K. Coot: model-building tools for molecular graphics. *Acta Crystallogr. D* **60,** 2126–2132 (2004).
55. Adams, P. D. *et al.* PHENIX: building new software for automated crystallographic structure determination. *Acta Crystallogr. D* **58,** 1948–1954 (2002).
56. Tang, G. *et al.* EMAN2: an extensible image processing suite for electron microscopy. *J. Struct. Biol.* **157,** 38–46 (2007).
57. Scheres, S. H. RELION: implementation of a Bayesian approach to cryo-EM structure determination. *J. Struct. Biol.* **180,** 519–530 (2012).
58. Radermacher, M., Wagenknecht, T., Verschoor, A. & Frank, J. Three-dimensional reconstruction from a single-exposure, random conical tilt series applied to the 50S ribosomal subunit of *Escherichia coli*. *J. Microsc.* **146,** 113–136 (1987).
59. Shaikh, T. R. *et al.* SPIDER image processing for single-particle reconstruction of biological macromolecules from electron micrographs. *Nature Protocols* **3,** 1941–1974 (2008).
60. Li, X. *et al.* Electron counting and beam-induced motion correction enable near-atomic-resolution single-particle cryo-EM. *Nature Methods* **10,** 584–590 (2013).
61. Mindell, J. A. & Grigorieff, N. Accurate determination of local defocus and specimen tilt in electron microscopy. *J. Struct. Biol.* **142,** 334–347 (2003).
62. Scheres, S. H. & Chen, S. Prevention of overfitting in cryo-EM structure determination. *Nature Methods* **9,** 853–854 (2012).
63. Chen, S. *et al.* High-resolution noise substitution to measure overfitting and validate resolution in 3D structure determination by single particle electron cryomicroscopy. *Ultramicroscopy* **135,** 24–35 (2013).
64. Voorhees, R. M., Fernández, I. S., Scheres, S. H. & Hegde, R. S. Structure of the mammalian ribosome-Sec61 complex to 3.4 Å resolution. *Cell* **157,** 1632–1643 (2014).
65. Greber, B. J. *et al.* The complete structure of the large subunit of the mammalian mitochondrial ribosome. *Nature* **515,** 283–286 10.1038/nature13895 (2014).
66. Brown, A. *et al.* Structure of the large ribosomal subunit from human mitochondria. *Science* **346,** 718–722 (2014).
67. Fernández, I. S., Bai, X. C., Murshudov, G., Scheres, S. H. & Ramakrishnan, V. Initiation of translation by cricket paralysis virus IRES requires its translocation in the ribosome. *Cell* **157,** 823–831 (2014).
68. Kucukelbir, A., Sigworth, F. J. & Tagare, H. D. Quantifying the local resolution of cryo-EM density maps. *Nature Methods* **11,** 63–65 (2014).
69. Pettersen, E. F. *et al.* UCSF Chimera – a visualization system for exploratory research and analysis. *J. Comput. Chem.* **25,** 1605–1612 (2004).
70. Emsley, P., Lohkamp, B., Scott, W. G. & Cowtan, K. Features and development of Coot. *Acta Crystallogr. D* **66,** 486–501 (2010).
71. Larkin, M. A. *et al.* Clustal W and Clustal X version 2.0. *Bioinformatics* **23,** 2947–2948 (2007).
72. Yachdav, G. *et al.* PredictProtein – an open resource for online prediction of protein structural and functional features. *Nucleic Acids Res.* **42,** W337–W343 (2014).
73. Bernsel, A., Viklund, H., Hennerdal, A. & Elofsson, A. TOPCONS: consensus prediction of membrane protein topology. *Nucleic Acids Res.* **37,** W465–W468 (2009).
74. Sonnhammer, E. L., von Heijne, G. & Krogh, A. A hidden Markov model for predicting transmembrane helices in protein sequences. *Proc. Int. Conf. Intell. Syst. Mol. Biol.* **6,** 175–182 (1998).
75. Tusnády, G. E. & Simon, I. The HMMTOP transmembrane topology prediction server. *Bioinformatics* **17,** 849–850 (2001).
76. Käll, L., Krogh, A. & Sonnhammer, E. L. Advantages of combined transmembrane topology and signal peptide prediction – the Phobius web server. *Nucleic Acids Res.* **35,** W429–W432 (2007).

©2015 Macmillan Publishers Limited. All rights reserved

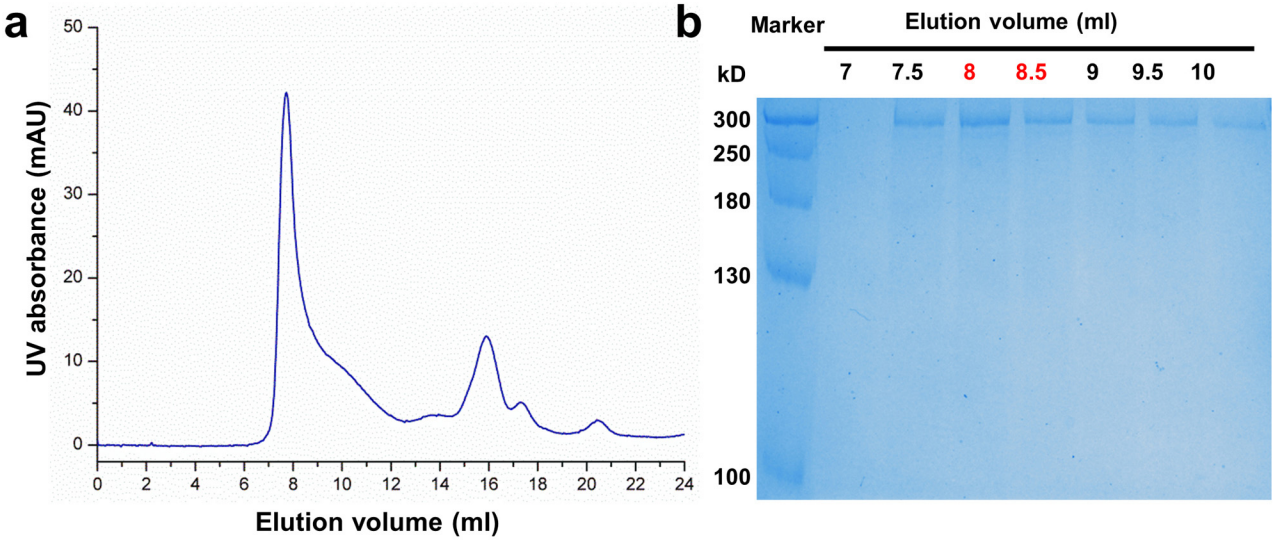

Extended Data Figure 1 | Biochemical characterization of the recombinant protein of Piezo1–pp–GST. **a**, A representative trace of gel filtration chromatography of the Piezo1–pp–GST protein. **b**, Protein samples of the indicated fractions were subjected to SDS–PAGE and Coomassie blue staining. Fractions of 8.0 ml and 8.5 ml (elution volume) were used for the negative-staining electron microscopy and native gel analyses, respectively.

©2015 Macmillan Publishers Limited. All rights reserved

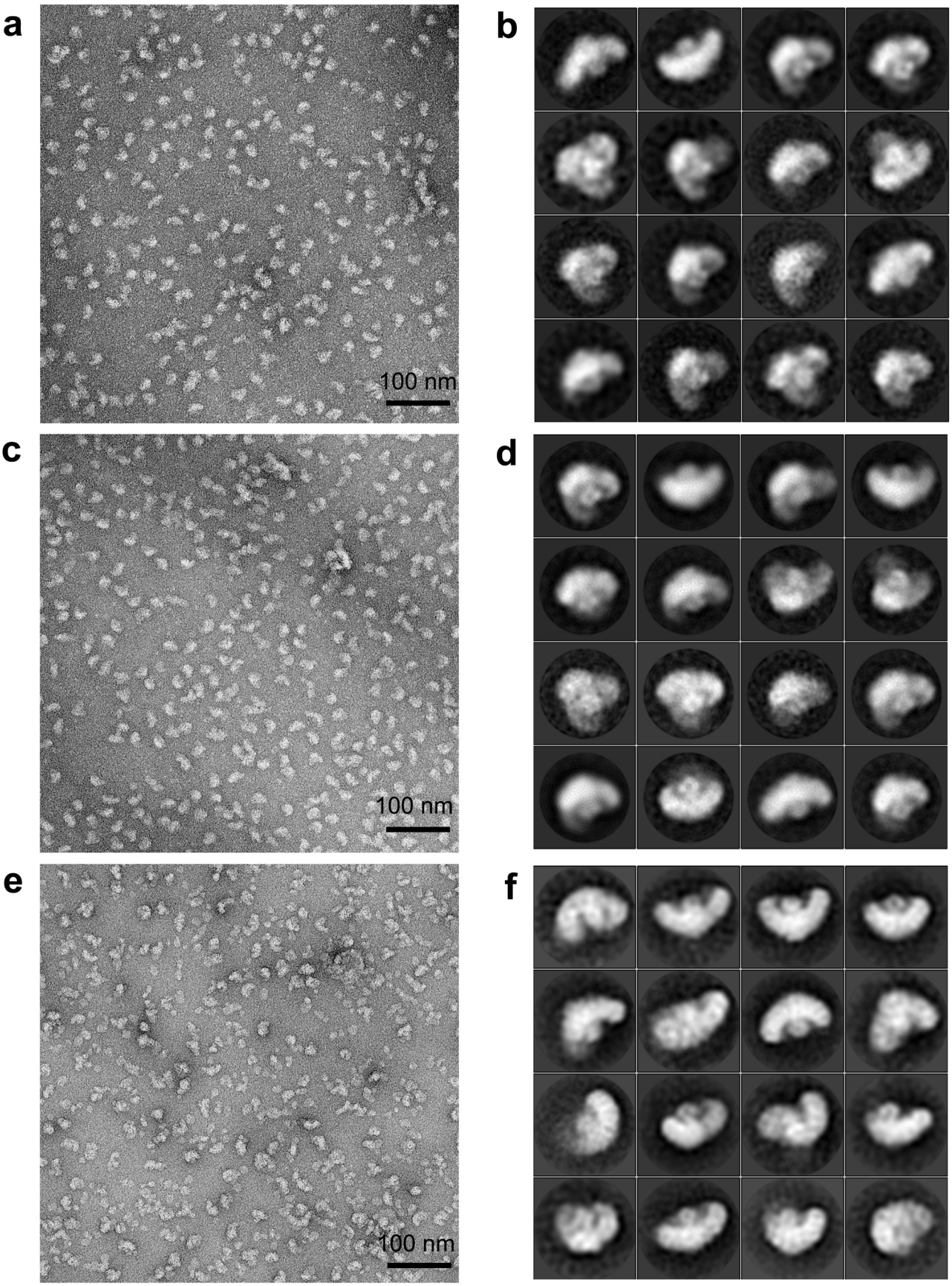

Extended Data Figure 2 | Negative-staining electron microscopy examination of Piezo1 in different detergents. **a**, A representative micrograph of negatively stained Piezo1 purified with C12E10. **b**, 2D class averages of Piezo1 particles (C12E10). **c**, A representative micrograph of negatively stained Piezo1 purified with C12E8. **d**, 2D class averages of Piezo1 particles (C12E8). **e**, A representative micrograph of negatively stained Piezo1, with amphipol A8-35 as detergent. **f**, 2D class averages of Piezo1 particles (amphipol A8-35).

©2015 Macmillan Publishers Limited. All rights reserved

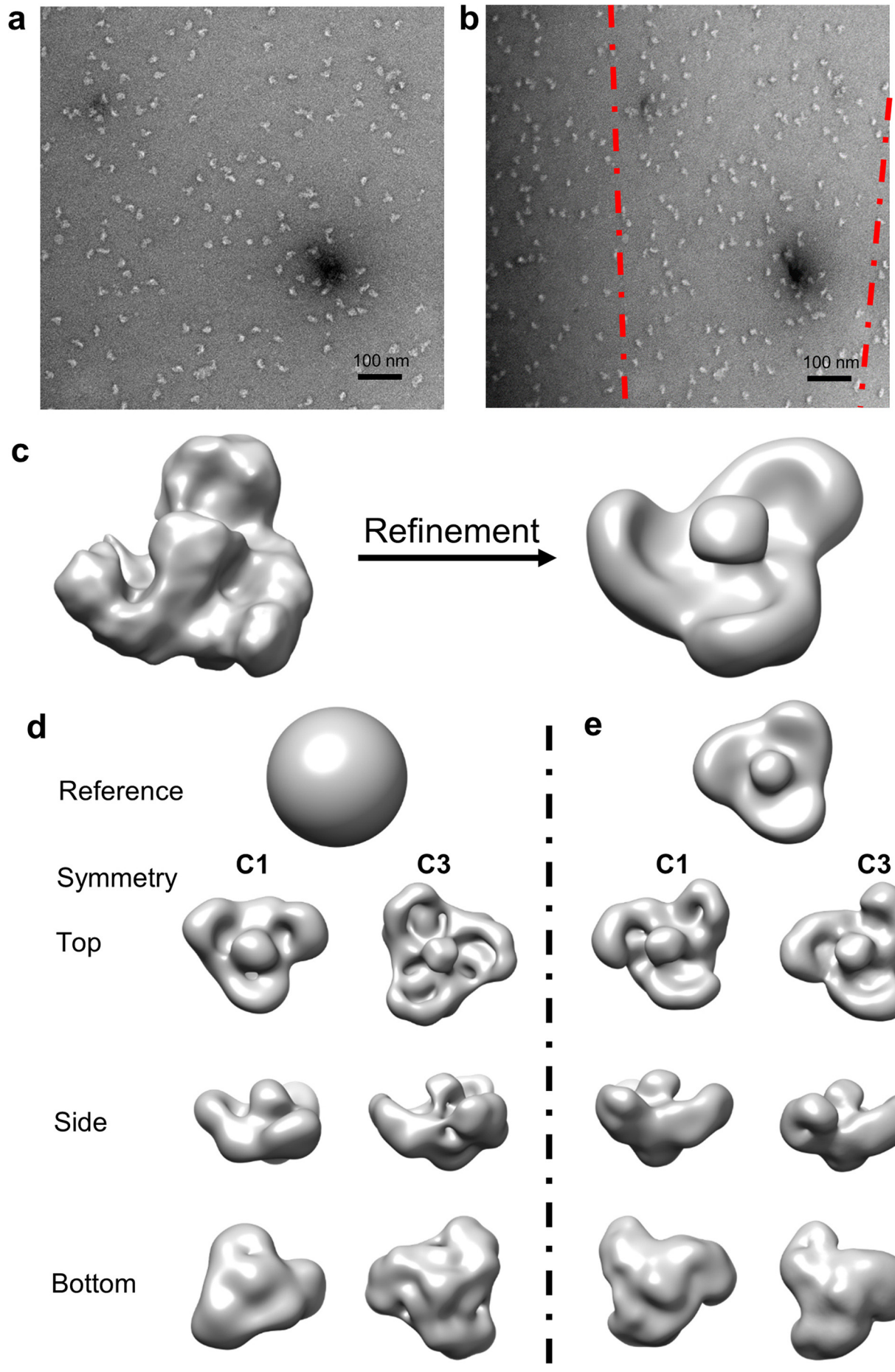

©2015 Macmillan Publishers Limited. All rights reserved

Extended Data Figure 3 | Initial model of Piezo1 generated from the random conical tilt method and validation of the model using cryo-electron microscopy data from a TF20 microscope. **a**, **b**, Representative micrographs of negatively stained Piezo1 in C12E10 collected in random conical tilt (RCT) pairs (**a**, untilted and **b**, 50° tilted). **c**, Top view of an RCT reconstruction, showing an overall threefold symmetry for the Piezo1 complex, is shown on the left. The right-hand side shows the top view of the refined model, obtained by a structural refinement of all particles from untilted micrographs. **d**, **e**, Model validation was performed by refinement of cryo-electron microscopy particles collected with TF20, with a Gaussian ball (**d**) or the RCT model (**e**) as initial reference. The 3D volumes are shown in top, side and bottom views. During the refinement, both the symmetry-free (C1) and symmetry-imposed (C3) reconstructions were tested. Note that some of these reconstructions have incorrect handedness.

©2015 Macmillan Publishers Limited. All rights reserved

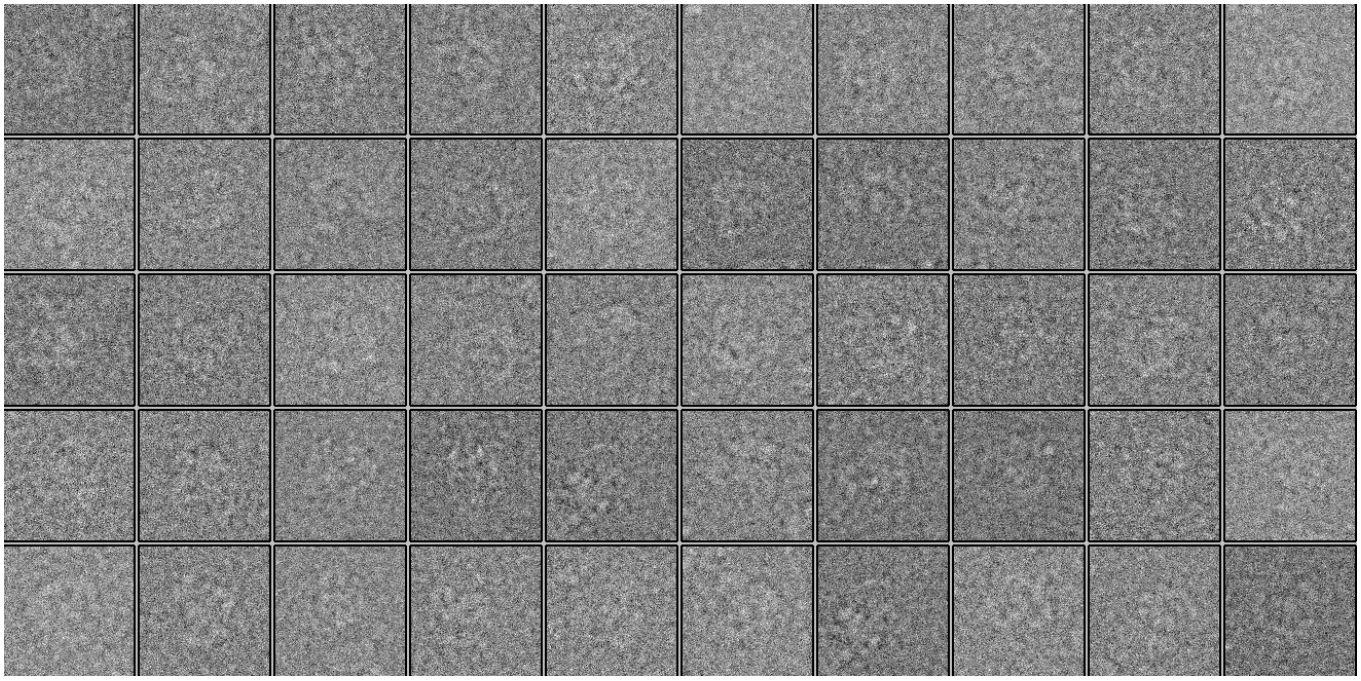

Extended Data Figure 4 | Representative raw particles of Piezo1 collected with the Titan Krios electron microscope fitted with a K2 electron detector. A collection of raw particles of Piezo1 (eluted with C12E10), collected with Titan Krios (300 kV).

©2015 Macmillan Publishers Limited. All rights reserved

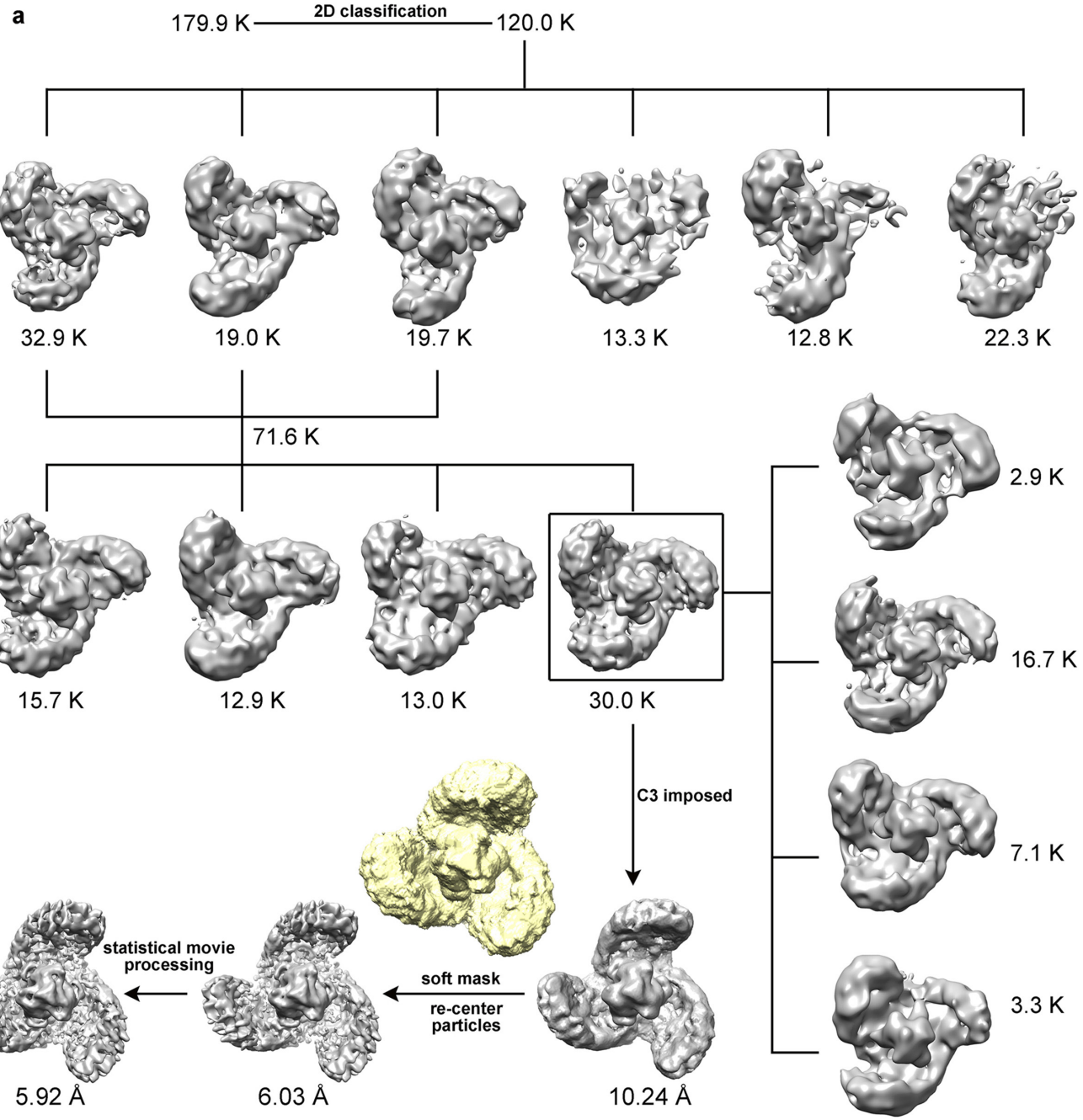

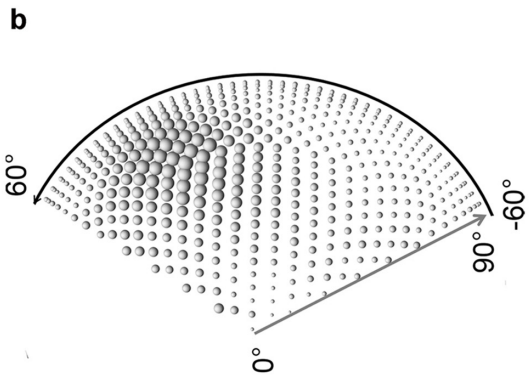

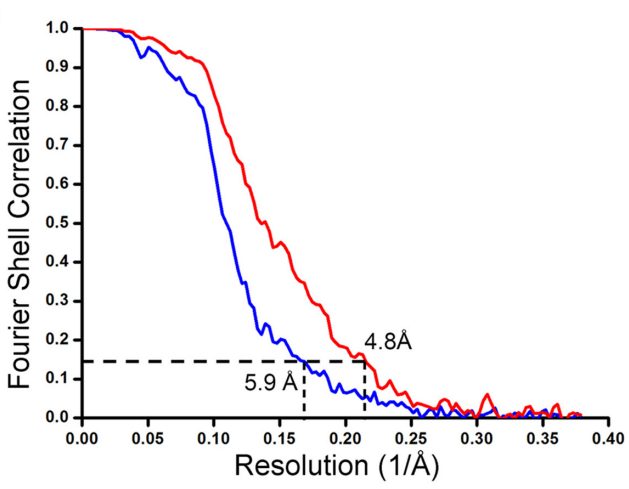

©2015 Macmillan Publishers Limited. All rights reserved

Extended Data Figure 5 | Workflow of 3D classification of Piezo1 particles. **a**, The schematic diagram of a series of 3D classification procedures with RELION is shown (also see Methods). After several rounds of 2D classification, the remaining 120,000 particles were subjected to three rounds of 3D classification without imposing any symmetry. A final set of particles (class 4 after the second round of 3D classification), with its reconstruction best matching threefold symmetry, was subjected to 3D refinement (C3 imposed). Notably, further 3D classification of this class resulted in generally similar structures (vertically arranged panels) without detectable improvement of conformational homogeneity. A top view of the soft mask used in structural refinement is also shown (yellow). **b**, Distribution of particle orientations in the last iteration of the refinement. **c**, Gold-standard Fourier shell correlation (FSC) curves of the final density map. The FSC curves were calculated with (red) or without (blue) the application of a soft mask to the two half-set maps. The final FSC curve (red) was corrected for the soft-mask-induced effect. Reported resolutions were based on FSC = 0.143 criteria.

©2015 Macmillan Publishers Limited. All rights reserved

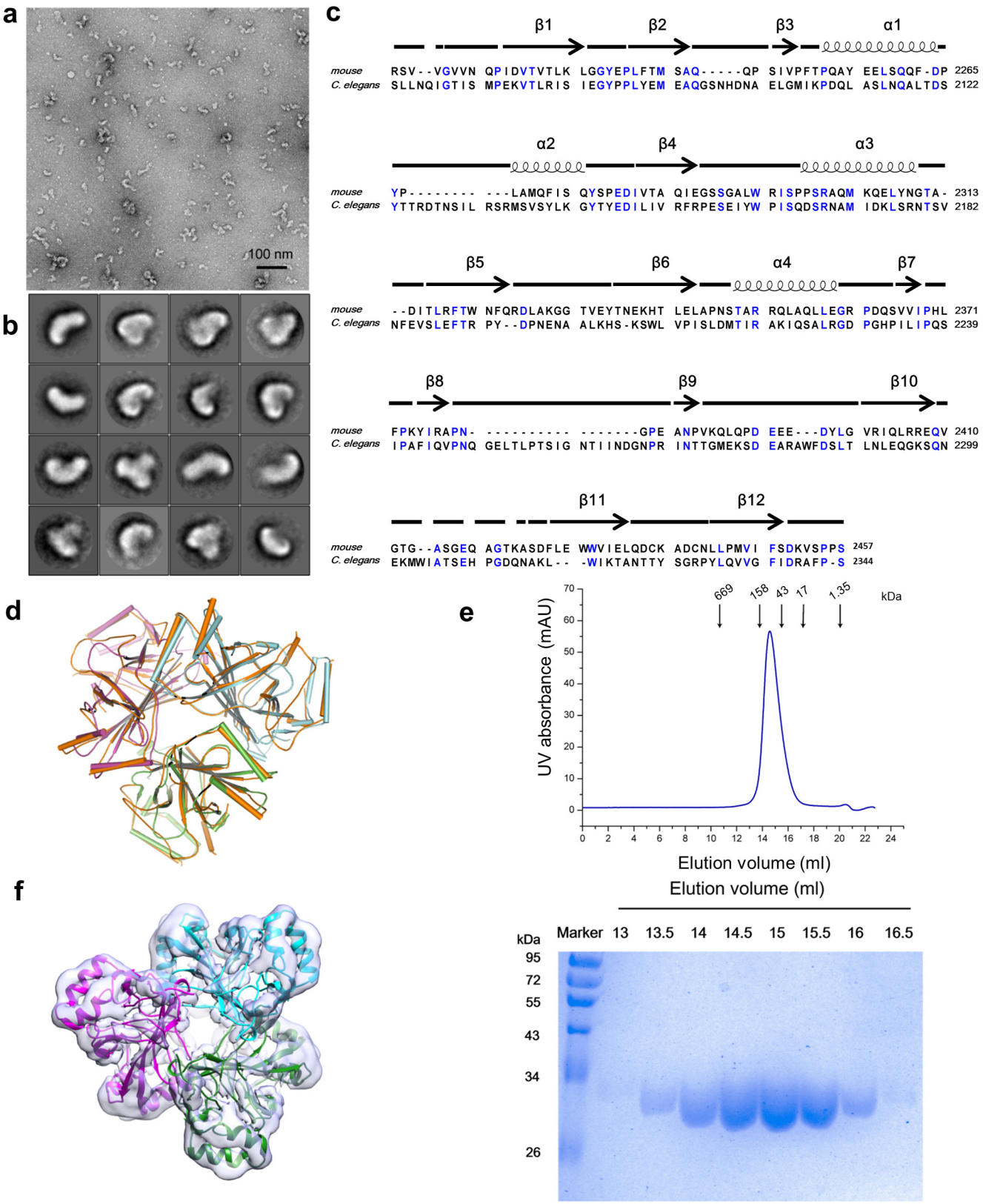

Extended Data Figure 6 | The trimeric CEDs form the cap domain of Piezo1. **a**, A representative micrograph of negatively stained Piezo1(ΔCED) in C12E10. **b**, 2D class averages of negatively stained Piezo1(ΔCED) particles. It is evident that the central cap domain is absent from these average images. **c**, Sequence alignment of the CED region of Piezo1 from *Mus musculus* and *Caenorhabditis elegans*. Identical residues are highlighted in blue. Secondary structures are indicated by cartoons above the primary sequence. Sequence alignment was performed using Clustal W2 (ref. 71). **d**, Structure alignment of the trimeric CED of Piezo1 from *M. musculus* and *C. elegans*. The three CEDs are coloured in purple, cyan and green, respectively. The CED of *C. elegans* is coloured in orange. **e**, A representative trace of gel filtration of the CED of Piezo1. The molecular weights are labelled. Protein samples of the indicated fractions were subjected to SDS–PAGE and Coomassie blue staining (bottom). **f**, Transparent surface representation of the segmented density map of the cap, superimposed with the trimeric CED crystal structure. The trimeric CEDs are coloured as in **d**.

©2015 Macmillan Publishers Limited. All rights reserved

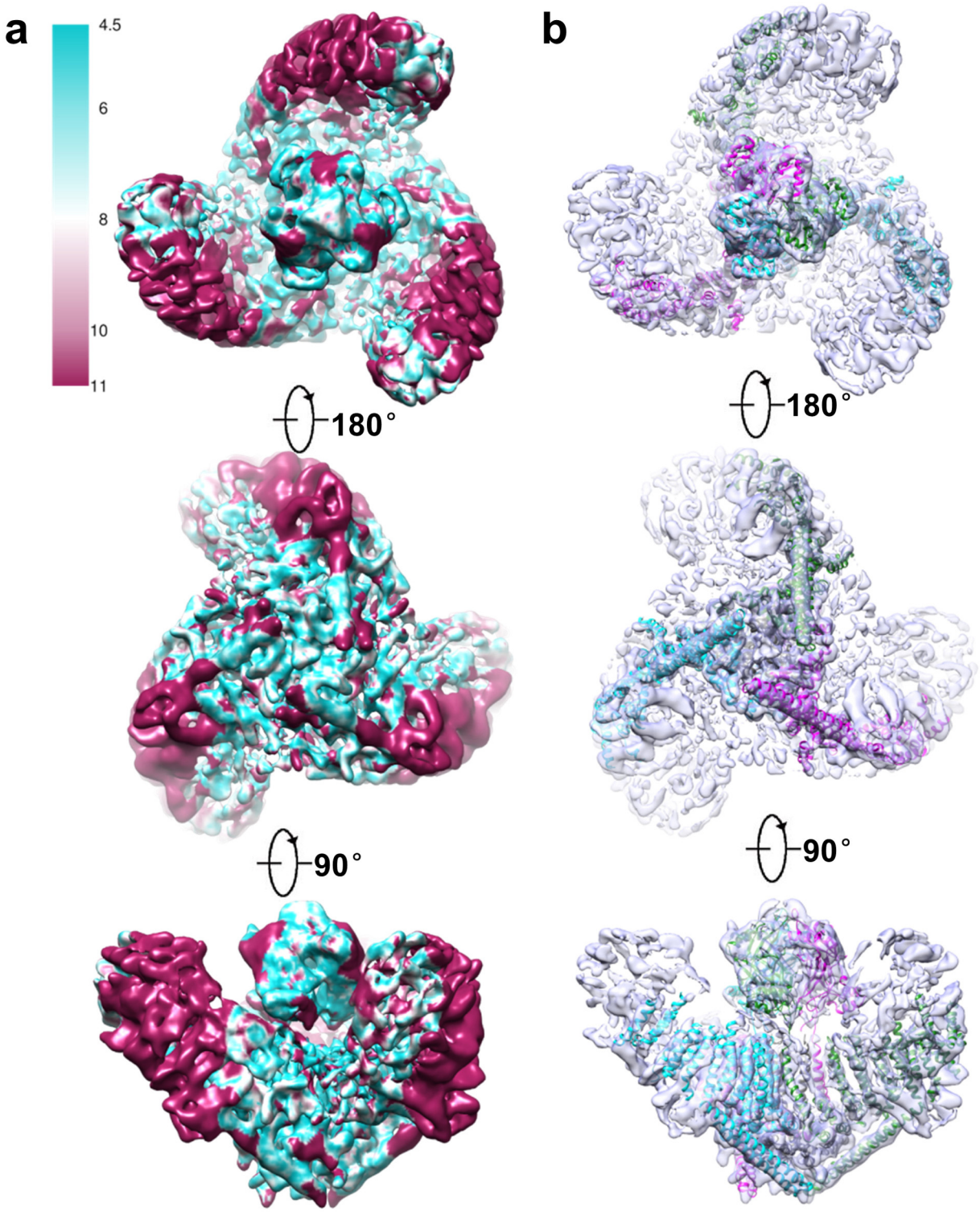

Extended Data Figure 7 | Local resolution map of the final density map. **a**, The final 3D density map of Piezo1 is coloured according to the local resolutions estimated by the software of ResMap. The density map is shown in three different views (top, bottom and side, respectively). **b**, The final 3D density map (transparent) is superimposed with a poly-alanine model and the crystal structure of the trimeric CED. Three protomers are coloured cyan, purple and green, respectively.

©2015 Macmillan Publishers Limited. All rights reserved

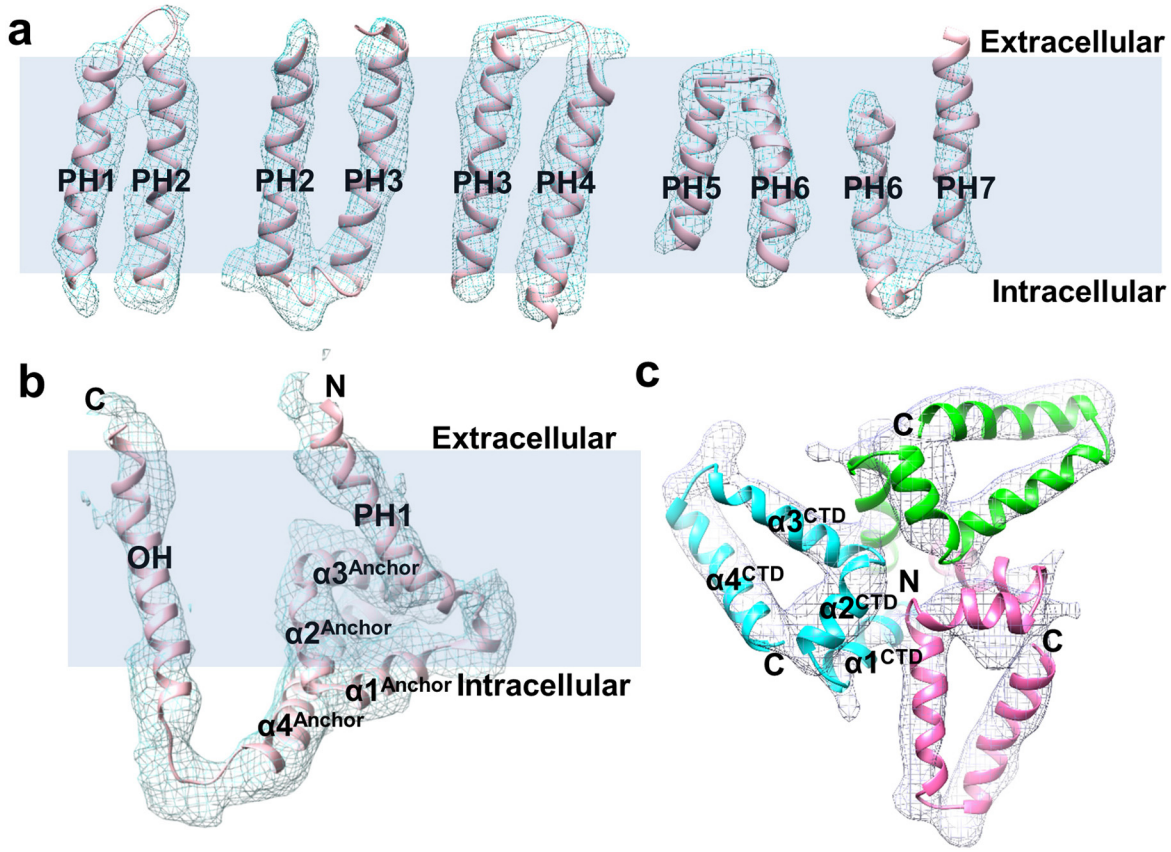

Extended Data Figure 8 | Density connections between the transmembrane helices and between the helices in the compact CTD. **a**, Alanine models of five representative pairs of transmembrane helices are displayed with their densities (mesh) superimposed. The transmembrane region is highlighted by a light purple shade with the intracellular and extracellular sides indicated. **b**, An alanine model of the anchor motif with its density superimposed (mesh). Four helices ($\alpha1^{anchor}$–$\alpha4^{anchor}$) connecting PH1 and OH are labelled. The transmembrane region is highlighted by a light purple shade with the intracellular and extracellular sides indicated. **c**, An alanine model of the last four helices ($\alpha1^{CTD}$–$\alpha4^{CTD}$) of the trimeric CTD, superimposed with the density of the CTD (mesh).

©2015 Macmillan Publishers Limited. All rights reserved

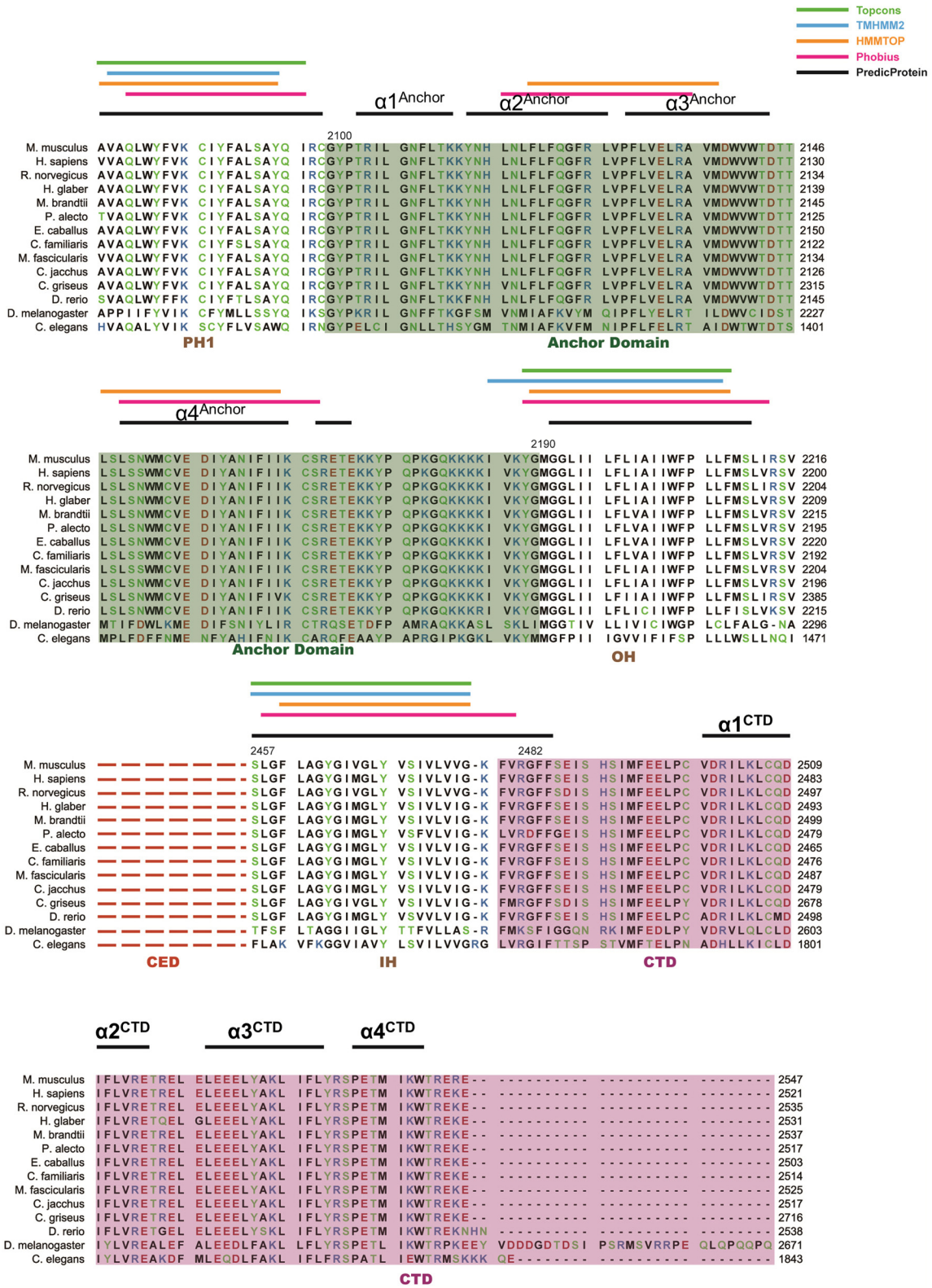

Extended Data Figure 9 | Secondary structure analyses of the C-terminal segments of Piezo1 proteins from different species. Sequence alignment of the C-terminal regions of Piezo1 from different species. The alignment was performed using Clustal W2 (ref. 71). The anchor motif and the CTD are highlighted in green and pink, respectively. For clarification, the sequences of CEDs were omitted and are indicated by red dashed lines. Secondary structures (α-helices) predicted with PredictProtein[72] are shown as black lines. Transmembrane segments were predicted using multiple web servers including Topcons[73] (green lines), TMHMM2 (ref. 74) (blue lines), HMMTOP[75] (orange lines) and Phobius[76] (pink lines).

©2015 Macmillan Publishers Limited. All rights reserved

Extended Data Table 1 | Statistics of data collection and structure refinement.

	Native	I-SAD
Data collection		
Diffraction beam	SSRF BL17U	BSRF 4W1B
Space Group	P213	P213
Unit Cell (Å)	a=b=c=89.492	a=b=c=89.766
Wavelength (Å)	0.979	1.700
Resolution (Å)	50.00-1.45 (1.50-1.45)	50.00-2.26 (2.34-2.26)
Rmerge (%)	9.2 (48.4)	25.7 (90.2)
I/σ	18.7 (4.0)	21.2 (2.1)
Completeness (%)	99.9 (100.0)	98.3 (82.8)
Redundancy	7.2 (7.1)	33.9 (7.4)
Wilson B factor (Å^2)	13.3	27.20
Refinement		
R_{work} (%)	15.15	
R_{free} (%)	17.59	
No. atoms		
Alll	2159	
Side chains	899	
Main chains	908	
Macromolecules	1807	
Solvent	352	
Average B-factor		
All	18.8	
Side chains	18.2	
Main chains	14.9	
Macromolecule	16.5	
Solvent	30.2	
RMS (bonds)	0.006	
RMS (angles)	1.065	
Ramachandran plot (%)		
Favored	98.21	
Allowed	1.79	
Outliers	0	

Values in parentheses are for the highest resolution shell. $R_{merge} = \Sigma_h\Sigma_i|I_{h,i}-I_h|/\Sigma_h\Sigma_i I_{h,i}$, where I_h is the mean intensity of the i observations of symmetry-related reflections of h. $R = \Sigma||F_{obs}|-|F_{calc}||/\Sigma|F_{obs}|$, where F_{calc} is the calculated protein structure factor from the atomic model (R_{free} was calculated with 5% of the reflections selected). I-SAD, single-wavelength anomalous dispersion of I atoms; BSRF, Beijing Synchrotron Radiation Facility; SSRF, Shanghai Synchrotron Radiation Facility.

©2015 Macmillan Publishers Limited. All rights reserved